

# Probing the electromagnetic response of dielectric antennas by vortex electron beams

Andrea Konečná,<sup>1,2</sup> Mikołaj K. Schmidt,<sup>1,3</sup> Rainer Hillenbrand,<sup>4</sup> and Javier Aizpurua<sup>1,5,\*</sup>

<sup>1</sup>Materials Physics Center, CSIC-UPV/EHU, 20018 Donostia-San Sebastián, Spain

<sup>2</sup>Central European Institute of Technology, Brno University of Technology, 612 00 Brno, Czech Republic

<sup>3</sup>Macquarie University Research Centre in Quantum Engineering (MQCQE), MQ Photonics Research Centre, Department of Physics and Astronomy, Macquarie University, NSW 2109, Australia.

<sup>4</sup>IKERBASQUE, Basque Foundation for Science, 48013 Bilbao, Spain

CIC NanoGUNE and UPV/EHU, 20018 Donostia-San Sebastián, Spain

<sup>5</sup>Donostia International Physics Center DIPC, 20018 Donostia-San Sebastián, Spain

(Dated: November 18, 2021)

Focused beams of electrons, which act as both sources, and sensors of electric fields, can be used to characterise the electric response of complex photonic systems, by locally probing the induced optical near fields. This functionality can be complemented by embracing the recently developed vortex electron beams (VEBs), made up of electrons with orbital angular momentum, which could in addition probe induced *magnetic* near fields. In this work we revisit the theoretical description of this technique, dubbed vortex Electron Energy-Loss Spectroscopy (v-EELS). We map the fundamental, quantum-mechanical picture of the scattering of the VEB electrons, to the intuitive classical models which treat the electron beams as superposition of linear electric and magnetic currents. We then apply this formalism to characterise the optical response of dielectric nanoantennas with v-EELS. Our calculations reveal that VEB electrons probe electric or magnetic modes with different efficiency, which can be adjusted by changing either beam vorticity or acceleration voltage, to determine the nature of the probed excitations. We also study a chirally-arranged nanostructure, which in the interaction with electron vortices produces dichroism in electron energy loss spectra. Our theoretical work establishes VEBs as versatile probes that could provide information on optical excitations otherwise inaccessible with conventional electron beams.

## I. INTRODUCTION

Electron energy-loss spectroscopy (EELS) in a scanning transmission electron microscope (STEM)<sup>1</sup> is an emerging technique to characterize optical excitations with high spatial and spectral resolution<sup>2–5</sup>. Recent experimental and theoretical studies have demonstrated capabilities of STEM-EELS to map near field of localized surface polaritons in plasmonic and phononic nanostructures that are of high interest in the field of nanophotonics for their applications in focusing and engineering light below the diffraction limit<sup>6,7</sup>.

An alternative possibility to control light at the nanoscale is to use resonant electromagnetic (EM) modes in nanoparticles made of materials with high refractive index<sup>8–13</sup>, which have been, however, relatively rarely studied by near-field spectroscopic methods<sup>14–19</sup>. It has been shown only by recent experiments that focused electron beams such as those used in STEM-EELS are capable to probe the response of dielectric antennas<sup>20–22</sup>. Here we explore the possibilities of using focused electron probes to distinguish electric and magnetic modes and *hot spots* that are crucial for applications of dielectric particles in nanophotonics<sup>23–27</sup>, and thus fully characterize the properties of their resonant modes.

Interestingly, besides conventional electron beams, recent efforts have led to generation of vortex electron beams (VEBs) in (S)TEM<sup>28–35</sup>. VEBs carry orbital angular momentum (OAM), which could facilitate direct interaction of the beam with excitations of both electric and magnetic nature. Besides various applica-

tions in probing magnetic fields<sup>36,37</sup>, magnetic transitions in bulk materials<sup>38–41</sup> and chirality of crystals<sup>42</sup>, the introduction of VEBs (and other shaped beams) in electron microscopy might also open a pathway for symmetry-based selective excitation of EM modes in photonic nanostructures<sup>43–45</sup>, separation of electric and magnetic modes<sup>46</sup>, or for developing the local investigation of the dichroic response of chiral nanoantennas<sup>45,47</sup>.

In this work, we show that STEM-EELS with the use of either a conventional or a vortex beam might be a suitable technique for distinguishing between the electric and magnetic nature of electromagnetic modes supported by dielectric antennas. We perform fully retarded calculations to retrieve the electromagnetic field arising from the electron-sample interaction and calculate EEL spectra, considering the interaction with electron beams of both zero and non-zero OAM. We study single and dimer dielectric antennas of different shapes, in particular spherical and cylindrical structures, made of silicon. We show that by varying excitation parameters or by comparing the spectra acquired with a non-vortex and a vortex beam, fast electrons preferentially couple to a specific type of modes. Finally, we explore dichroism in the EEL signal emerging when the VEB interacts with a chiral dielectric nanostructure.

## II. THEORETICAL FRAMEWORK FOR VORTEX ELECTRON ENERGY LOSS SPECTROSCOPY AT OPTICAL FREQUENCIES

We first introduce the theoretical approach for calculating the interaction between VEBs and optical excitations in arbitrarily shaped nanostructures in the framework of classical electrodynamics (see further discussion and comparison with the quantum-mechanical formalism in Appendix A). To facilitate fully retarded calculations of EEL spectra, needed to capture interactions of both electric and magnetic nature, we consider VEBs in the perfect-focus limit. Such simplified scenario allows us to approximate the VEB as a superposition of a frequency-dependent electric line current, expressed as

$$\mathbf{J}_e = -e e^{\frac{i\omega z}{v}} \mathbf{e}_z, \quad (1)$$

and a magnetic current (see Appendix B), as

$$\mathbf{J}_m = \frac{il\omega \mu_B}{v} e^{i\omega z/v} \mathbf{e}_z, \quad (2)$$

where  $\mathbf{e}_z$  denotes direction of the optical axis,  $e$  is the elementary charge,  $v$  is the electron's speed determined by the acceleration voltage,  $\mu_B = e\hbar/(2m_e)$  is the Bohr's magneton with the electron mass  $m_e$  and  $\hbar$  is the reduced Planck's constant. Vorticity of the beam is characterized by the orbital angular momentum (OAM)  $\hbar l$  ( $l = 0$  for a non-vortex beam).

Within classical electrodynamics, the line currents above can be considered as external sources inducing the electromagnetic response of a sample, which acts back on the electron beam and causes its energy loss<sup>2</sup>. The total energy loss consists of the energy loss experienced by both the electric and the magnetic current components of the beam:  $\Delta E = \Delta E_e + \Delta E_m$ . By using the invariance of Maxwell's equations under the transformation

$$\mathbf{E} \rightarrow -c\mathbf{B}, \quad \mathbf{B} \rightarrow \frac{\mathbf{E}}{c}, \quad \mathbf{J}_e \rightarrow \frac{\mathbf{J}_m}{c}, \quad (3)$$

where we considered the relative permeability  $\mu = 1$ , the electric and the magnetic energy losses in the non-recoil approximation are given by<sup>46</sup>

$$\Delta E_{\{e/m\}} = \frac{\{\mp\}}{\pi} \int_0^\infty d\omega \int_{-\infty}^\infty dz \times \text{Re} \left[ \{E/B\}_z^{\text{ind}}(z, \omega) J_{\{e/m\}, z}^*(z, \omega) \right], \quad (4)$$

where  $E_z^{\text{ind}}$  and  $B_z^{\text{ind}}$  are the  $z$  components of the induced electric and the magnetic field, respectively. The field components depend on the angular frequency  $\omega$ , and are evaluated at the electron's trajectory along the  $z$  axis.

We can now introduce the electric and magnetic loss probabilities  $\Gamma_e$  and  $\Gamma_m$ , respectively, as  $\Delta E_{\{e/m\}} = \int_0^\infty d\omega \hbar\omega \Gamma_{\{e/m\}}$ . The total loss probability

$$\Gamma(\omega) = \Gamma_e(\omega) + \Gamma_m(\omega) \quad (5)$$

then corresponds to the measured electron energy loss spectrum for the case that a perfectly focused VEB is employed and that we disregard OAM exchange. By inserting the current densities from Eq. (1) and Eq. (2) into Eqs. (4), the probabilities can be expressed as  $\Gamma_e = \Gamma_{e, \mathbf{J}_e} + \Gamma_{e, \mathbf{J}_m}$  and  $\Gamma_m = \Gamma_{m, \mathbf{J}_m} + \Gamma_{m, \mathbf{J}_e}$ , where

$$\Gamma_{e, \mathbf{J}_{\{e/m\}}} = \frac{e}{\pi \hbar \omega} \int_{-\infty}^\infty dz \text{Re} \left[ E_{z, \mathbf{J}_{\{e/m\}}}^{\text{ind}}(z, \omega) e^{-\frac{i\omega z}{v}} \right], \quad (6)$$

$$\Gamma_{m, \mathbf{J}_{\{e/m\}}} = \frac{l \mu_B}{\pi \hbar v} \int_{-\infty}^\infty dz \text{Im} \left[ B_{z, \mathbf{J}_{\{e/m\}}}^{\text{ind}}(z, \omega) e^{-\frac{i\omega z}{v}} \right]. \quad (7)$$

We split the induced electric field excited by the electric and the magnetic current ( $\mathbf{E}_{\mathbf{J}_e}^{\text{ind}}$  and  $\mathbf{E}_{\mathbf{J}_m}^{\text{ind}}$ ), yielding the corresponding loss probabilities  $\Gamma_{e, \mathbf{J}_e}$  and  $\Gamma_{e, \mathbf{J}_m}$ , respectively. Similarly, the induced magnetic field originates from the interaction of the sample with both current sources ( $\mathbf{B}_{\mathbf{J}_e}^{\text{ind}}$  and  $\mathbf{B}_{\mathbf{J}_m}^{\text{ind}}$ ), giving rise to the loss channels  $\Gamma_{m, \mathbf{J}_e}$  and  $\Gamma_{m, \mathbf{J}_m}$ . Note that the electric loss probability  $\Gamma_{e, \mathbf{J}_e}$  in Eq. (6) corresponds to the conventional EEL spectrum obtained for a beam with  $l = 0$ .

## III. RESULTS AND DISCUSSION

In the following, we present calculations of the loss probabilities [Eqs. (6) and (7)] for different sample geometries where we solve for the induced EM field either analytically or numerically (as described in Appendix C).

### A. Spectroscopy of localized modes in spherical dielectric nanoantennas

We first apply the theory presented above to the canonical example of a single spherical nanoparticle. Due to its symmetry, the terms  $\Gamma_{e, \mathbf{J}_m}$  and  $\Gamma_{m, \mathbf{J}_e}$  do not contribute to the loss probability and we need to evaluate only the terms  $\Gamma_{e, \mathbf{J}_e}$  and  $\Gamma_{m, \mathbf{J}_m}$ . The fully-retarded analytical solution of the induced electric field arising from the excitation of a spherical particle by an electric current was obtained in Ref.<sup>48</sup>, and the corresponding EEL probability is expressed as:

$$\Gamma_e^{\text{sph}} \rightarrow \Gamma_{e, \mathbf{J}_e} = \frac{e^2}{4\pi\epsilon_0 c \hbar \omega} \sum_{n=1}^\infty \sum_{m=-n}^n K_m^2 \left( \frac{\omega b}{v \gamma_L} \right) \times [C_{n,m}^M \text{Im}[t_n^M] + C_{n,m}^E \text{Im}[t_n^E]], \quad (8)$$

where  $\epsilon_0$  is the vacuum permittivity, the summation is performed over multipoles  $(n, m)$ ,  $K_m(x)$  is the modified Bessel function of the second kind of order  $m$ ,  $b$  is the distance of the beam from the center of the sphere (the impact parameter), and the coefficients  $C_{n,m}^{\text{E/M}}$  take into account the coupling with the field of the electron beam

(see Eqs. (30) and (31) of Ref.<sup>48</sup>). We use superscripts M/E to denote the coefficients related to the excitation of the magnetic/electric modes. Eq. (8) also includes the Mie coefficients:

$$t_n^M = i \frac{j_n(ka)[k_{in}aj_n(k_{in}a)]' - j_n(k_{in}a)[kaj_n(ka)]'}{h_n^{(1)}(ka)[k_{in}aj_n(k_{in}a)]' - j_n(k_{in}a)[kah_n^{(1)}(ka)]'}, \quad (9)$$

$$t_n^E = i \frac{j_n(ka)[k_{in}aj_n(k_{in}a)]' - \varepsilon j_n(k_{in}a)[kaj_n(ka)]'}{h_n^{(1)}(ka)[q_{in}aj_n(k_{in}a)]' - \varepsilon j_n(k_{in}a)[kah_n^{(1)}(ka)]'}, \quad (10)$$

where  $k = \omega/c$  is the magnitude of the wave vector in vacuum,  $k_{in} = \sqrt{\varepsilon}\omega/c$  the wave vector inside the sphere characterized by relative dielectric function  $\varepsilon$ , and  $a$  is radius of the sphere.  $j_n(x)$  and  $h_n^{(1)}(x)$  are the spherical Bessel and Hankel functions of the first kind, respectively. The derivatives in Eq. (9) and Eq. (10) are performed with respect to the functions' arguments.

When we consider the excitation of the sphere by a magnetic current, the corresponding loss probability  $\Gamma_m^{\text{sph}}$  can be readily obtained by utilizing the transformation given by Eq. (3). The magnetic-current-mediated loss probability is thus given by

$$\Gamma_m^{\text{sph}} \rightarrow \Gamma_{m,J_m} = \left( \frac{l \mu_B}{v} \right)^2 \frac{\mu_0 \omega}{4\pi c \hbar} \times \sum_{n=1}^{\infty} \sum_{m=-n}^n K_m^2 \left( \frac{\omega b}{v \gamma} \right) [C_{n,m}^M \text{Im}[t_n^E] + C_{n,m}^E \text{Im}[t_n^M]]. \quad (11)$$

We now explore whether we can distinguish modes of electric and magnetic nature excited in silicon nanoparticles with help of the VEB-EEL spectra. In Fig. 1(a,b) we show the calculated spectral contributions  $\Gamma_e^{\text{sph}}$  [Eq. (8); solid red line] and  $\Gamma_m^{\text{sph}}$  [Eq. (11); solid blue line], respectively, for a single silicon nanosphere with radius  $a = 150$  nm, an impact parameter  $b = 157.5$  nm [as depicted in the inset of Fig. 1(b)] and considering a 100 keV beam ( $v = 0.548c$ ). We note that while the spectrum in (a) does not depend on  $\hbar l$  and thus is identical for a vortex and non-vortex beam,  $\Gamma_m$  in (b) is nonzero only for a vortex beam. We considered  $|l| = 100$  for our vortex beam.

To understand the origin of the resulting spectral features, we split the full spectra (solid lines) into the contributions of the different electric ( $E_n$ ) or magnetic ( $M_n$ )  $n$ -order multipoles (dashed lines), *i.e.*, the spectra in Eqs. (8) and (11) before the summation over  $n$ . In the considered spectral range, the probability  $\Gamma_e^{\text{sph}}$  [solid red line in Fig. 1(a)] exhibits four well distinguishable peaks, which arise due to the excitation of a magnetic dipolar mode (M1, dark blue dashed line), electric dipole (E1, light red dashed line), magnetic quadrupole (M2, light blue dashed line) and electric quadrupole (E2, orange dashed line), whose energy nearly coincides with

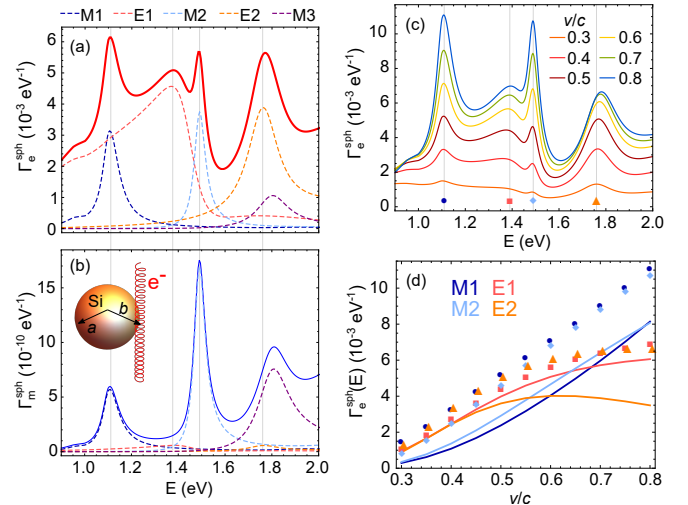


FIG. 1: (a) EEL probability,  $\Gamma_e^{\text{sph}}$ , as calculated by evaluation of Eq. (8) (solid red line) for an electron of energy 100 keV ( $v = 0.548c$ ) interacting with a silicon spherical particle of radius  $a = 150$  nm at an impact parameter  $b = 157.5$  nm (see the inset of (b) for the geometrical arrangement). The dielectric function of amorphous silicon is taken from Ref. <sup>49</sup>. (b) Magnetic-current mediated loss probability,  $\Gamma_m^{\text{sph}}$ , as calculated by evaluation of Eq. (11), for the same parameters as in (a), and considering OAM  $\hbar l = 100\hbar$  (solid blue line). Contributions to the loss probabilities from different electromagnetic modes are split in (a,b): magnetic dipole (M1, dark blue dashed line), electric dipole (E1, light red dashed line), magnetic quadrupole (M2, light blue dashed line), electric quadrupole (E2, orange dashed line), and magnetic octupole (M3, purple dashed line). Notice the different intensity scale of (b). (c)  $\Gamma_e^{\text{sph}}$  evaluated for varying electron's velocity  $v$ . (d) Intensities of the peaks marked in (c) (colored symbols), with the color-coding corresponding to the dashed lines in (a,b). The contribution to the intensity of each electromagnetic mode is also displayed by solid lines with the same color code as in (a,b).

the magnetic octupole (M3, purple dashed line). On the other hand, due to the interchange of the coupling coefficients [compare Eq. (8) *vs.* Eq. (11)], only the magnetic modes (M1, M2 and M3) are found in the plot of  $\Gamma_m^{\text{sph}}$  [solid blue line in Fig. 1(b)]. The cross-coupling of the magnetic current to the electric modes is negligible and produces only a small contribution [see dashed light red and orange lines in Fig. 1(b) close to zero].

In a typical measurement of EELS, one obtains the total loss probability  $\Gamma^{\text{sph}} = \Gamma_e^{\text{sph}} + \Gamma_m^{\text{sph}}$  [sum of solid spectra in (a) and (b)]. Therefore, in order to separate the loss probability components  $\Gamma_e^{\text{sph}}$  and  $\Gamma_m^{\text{sph}}$ , two measurements would be needed: one with a beam where  $l \neq 0$  and another one with exactly the same experimental conditions with a non-vortex beam ( $l = 0$ ). After subtraction of these two spectra, one would obtain  $\Gamma_m^{\text{sph}}$ , which only shows the peaks corresponding to the magnetic modes. Unfortunately, we can observe that even for relatively large OAM, the *magnetic* part of the loss prob-

ability  $\Gamma_m^{\text{sph}}$  is six orders of magnitude smaller than  $\Gamma_e^{\text{sph}}$ , and thus falls below the limit of the currently achievable signal-to-noise ratio in STEM-EELS experiments.

In addition to varying the OAM of the VEB, there is an additional degree of freedom, which might be used to assign the spectral peaks to the modes as either electric or magnetic: the electron's speed  $v$  which governs the strength of the coupling coefficients  $C_{n,m}^{\text{E/M}}$  related to the electromagnetic field of the fast electrons. In Fig. 1(c) we evaluate  $\Gamma_e^{\text{sph}}$  for varying  $v$  and  $l = 0$  (conventional electron beam). We observe that the intensity ratio of the four visible peaks changes significantly. With increasing accelerating voltage (electron's speed), the coupling of the beam with the magnetic modes is much more efficient, which results from the fact that the accompanying magnetic field is stronger for faster electrons. Further, the intensity corresponding to the excitation of the M1 and M2 modes grows faster than the peak assigned to the E1 mode, which starts to saturate for larger speeds ( $v > 0.7c$ ). This trend is confirmed in Fig. 1(d), where we plot the intensities of the peaks extracted from spectra in Fig. 1(c) at the energies corresponding to the M1 (dark blue points), E1 (light red squares), M2 (light blue diamonds), and E2 (orange triangles) modes, depending on the electron's speed. We also plot the peak intensities as if the modes were excited independently by solid lines to eliminate the influence of the spectral overlap of the excited modes [see Fig. 1(a) showing that, *e.g.*, E1 contributes significantly even at the energy of the M1 peak]. This trend is similar for higher-order modes and we suggest that obtaining the EEL spectra at several acceleration voltages might serve for a relatively straightforward classification of the modes.

VEBs can also be applied to unravel the spectral response of more complex dielectric nanostructures, such as dimers of two (identical) particles separated by a small gap. The nanoparticle dimers are also of large interest as they can provide a significant enhancement of the field in the gap or yield directional scattering<sup>12,14,50,51</sup>. In Fig. 2 we thus study numerically VEB-EELS of a pair of spherical dielectric particles (each of them with the same properties as the single spherical particle studied in Fig. 1) separated by a gap of distance  $g = 15$  nm. It has been shown that in such a system, the modes of the individual particles hybridize and form bonding and anti-bonding modes of the dimer<sup>52</sup>. In Fig. 2(a,b) we analyze how these hybridized modes contribute to the spectra for different VEB positions.

In Fig. 2(a) we consider a 100-keV electron beam with  $|l| = 100$  passing through the middle of the gap and calculate the EEL probability. We note that the crossed loss probability components  $\Gamma_{e,J_m}$  and  $\Gamma_{m,J_e}$  are either identically zero or cancel. We can thus again assign  $\Gamma_e \rightarrow \Gamma_{e,J_e}$  and  $\Gamma_m \rightarrow \Gamma_{m,J_m}$ . Importantly, the symmetry of the electric or magnetic field produced by the electric or magnetic part of VEB current dictates which current component couples to specific modes of the dimer. We schematically depict possible scenarios next to the graph.  $\Gamma_e$

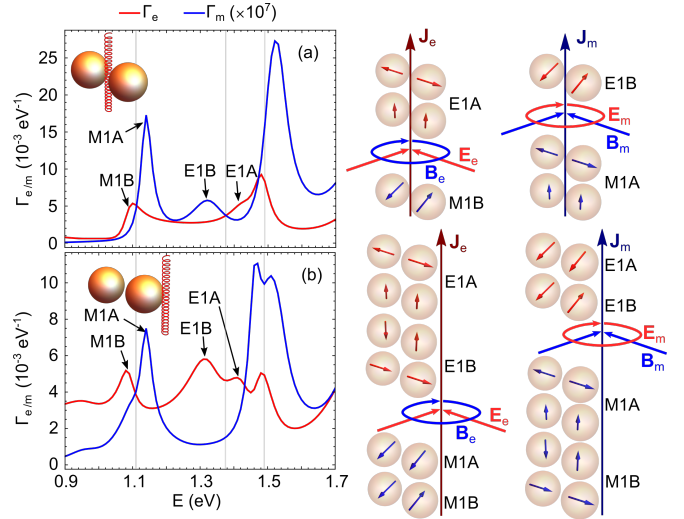


FIG. 2: (a,b) Numerically calculated electric-current and magnetic-current-mediated EEL probabilities,  $\Gamma_e$  (solid red line) from Eq. (6), and  $\Gamma_m$  (solid blue line) from Eq. (7), respectively, for a 100-keV electron beam with  $l = 100$  exciting a spherical particle dimer. Each spherical particle of radius  $a = 150$  nm is made of silicon (dielectric response is taken from Ref. <sup>49</sup>). The distance of the gap between the particles is  $g = 15$  nm and the beam is passing either (a) through the middle of the gap or (b) by the side of one of the particles at the axis of the dimer, 7.5 nm from its surface. We denote the loss peaks corresponding to the hybridized dipolar modes in the dimer as: bonding and antibonding magnetic dipole (M1B and M1A), and bonding and antibonding electric dipole (E1B and E1A). Gray vertical lines denote spectral positions of the modes M1, E1 and M2 in the EEL spectra calculated for a single spherical particle (see Fig. 1). Next to the corresponding spectra, electric (red arrows) and magnetic (blue arrows) coupled-dipole configurations excitable by each of the current contributions is schematically depicted.

[solid red line in Fig. 2(a)] shows that the electric current component can excite the magnetic dipolar bonding mode (M1B), the electric antibonding mode (E1A), and the bonding magnetic quadrupolar mode yielding a peak close to 1.5 eV. On the other hand, the magnetic part of the current couples to the magnetic dipolar anti-bonding mode (M1A), the electric dipolar bonding mode (E1B) and the anti-bonding magnetic quadrupolar mode (see the peak above 1.5 eV), which appears in  $\Gamma_m$  [solid blue line in Fig. 2(a)]. The energy splitting of the bonding and anti-bonding modes is apparent when the peak positions are compared to the spectral positions of the modes excited in the individual sphere (plotted by vertical gray lines, extracted from Fig. 1).

When the beam is moved to the side of one of the spheres along the dimer axis [see the schematics in Fig. 2(b)], bonding and anti-bonding dipolar modes are excitable by both current components as schematically shown next to the graph. However, some of the dipolar arrangements are excited preferentially, which is appar-

ent in the respective spectra. The electric component of the current efficiently couples with the M1B mode, E1A mode and also E1B mode [solid red line in Fig. 2(b)]. On the other hand,  $\Gamma_m$  [solid blue line in Fig. 2(b)] shows a spectral feature arising from the excitation of both M1A and M1B. Interestingly, M1A is dominant with respect to M1B, whose excitation gives rise to a small shoulder below 1.1 eV. We also observe that the magnetic current component couples only weakly to the E1B and E1A mode. However, we note that this loss contribution is still six to seven orders of magnitude smaller than the electric part and would be difficult to isolate as discussed above.

## B. Probing the photonic density of states in an infinite cylinder

Another canonical example of a dielectric system with a strong electric and magnetic response, which can

be characterized via VEB-EELS, is that of dielectric waveguides<sup>23,53–57</sup>. Previous theoretical analysis of the interaction of fast electrons with dielectric cylindrical waveguides has already suggested their potential for applications in single-photon sources<sup>58</sup>. Here we study the EEL probability of a VEB exciting an infinite cylindrical wire of radius  $a$  placed in vacuum. We consider a geometrical arrangement as sketched in Fig. 3: an electron beam moving at speed  $v$  parallel to the axis of the wire at a distance  $b > a$  from the center of the cylinder. For this geometry, the retarded analytical solution of the EEL probability was presented *e.g.* in Ref.<sup>59</sup> and reproduced in Appendix C, which we can easily modify to include the contribution to the loss experienced by the magnetic component of the current by using the transformation in Eq. (3). We can write the two contributions to the overall loss probability of the VEB per unit length as:

$$\frac{d\Gamma_e}{dz} = \frac{d\Gamma_{e,J_e}}{dz} = \frac{e^2}{2\pi^2\hbar\omega^2\epsilon_0} \underbrace{\sum_{m=0}^{\infty} \text{Re} \{ (2 - \delta_{m0}) K_m(\Omega_o b) (q_z^2 - k^2) b_{e,m}(q_z, \omega) \}}_{\gamma_e(q_z, \omega)}|_{q_z = \frac{\omega}{v}}, \quad (12)$$

$$\frac{d\Gamma_m}{dz} = \frac{d\Gamma_{m,J_m}}{dz} = \frac{\mu_B^2 l^2 \mu_0}{2\pi^2 v^2 \hbar} \underbrace{\sum_{m=0}^{\infty} \text{Re} \{ (2 - \delta_{m0}) K_m(\Omega_o b) (q_z^2 - k^2) d_{m,m}(q_z, \omega) \}}_{\gamma_m(q_z, \omega)}|_{q_z = \frac{\omega}{v}}, \quad (13)$$

where  $m$  denotes different azimuthal modes,  $\delta_{m0}$  is the Kronecker delta, and  $q_z$  stands for the wavevector along the axis of the cylinder which has to match the wavevector component transferred from the fast electron  $q_z = \omega/v$ . The dimensionless coefficients  $b_e(q_z, \omega)$  and  $d_m(q_z, \omega)$  can be obtained as described in Appendix C.

We also define  $\Omega_o = \sqrt{q_z^2 - k^2}$ .

The denominators of the coefficients  $b_m$  and  $d_m$  yield the dispersion of all the modes supported by the cylinder with relative dielectric function  $\epsilon$ :

$$\begin{aligned} \frac{k^2 q_z^2 m^2}{a^2 \Omega_o^4 \Omega_i^2} K_m(\Omega_o a)^2 I_m(\Omega_i a)^2 (\epsilon - 1)^2 + \left[ \frac{\Omega_i}{\Omega_o} I_m(\Omega_i a) K'_m(\Omega_o a) - K_m(\Omega_o a) I'_m(\Omega_i a) \right] \\ \times \left[ \epsilon K_m(\Omega_o a) I'_m(\Omega_i a) - \frac{\Omega_i}{\Omega_o} I_m(\Omega_i a) K'_m(\Omega_o a) \right] = 0, \end{aligned} \quad (14)$$

where  $I_m(x)$  and  $K_m(x)$  are the modified Bessel functions of the first and the second kind, respectively, of order  $m$ , and  $\Omega_i = \sqrt{q_z^2 - k_{in}^2}$ , where  $k_{in} = \sqrt{\epsilon\omega/c}$  is the wave vector inside the cylinder.

In Fig. 3(a,b) we plot the  $(q_z, \omega)$ -dependent loss probabilities  $\gamma_e$  and  $\gamma_m$  as implicitly defined in Eq. (12)

and Eq. (13), respectively, for geometrical parameters  $a = 150$  nm and  $b = 160$  nm. On top of the density plots we show the dispersion curves corresponding to the guided EM modes (the leaky modes above the light line, given by  $q_z = \omega/c$ , are not shown as they are not excitable by the parallel beam) supported by the infinite

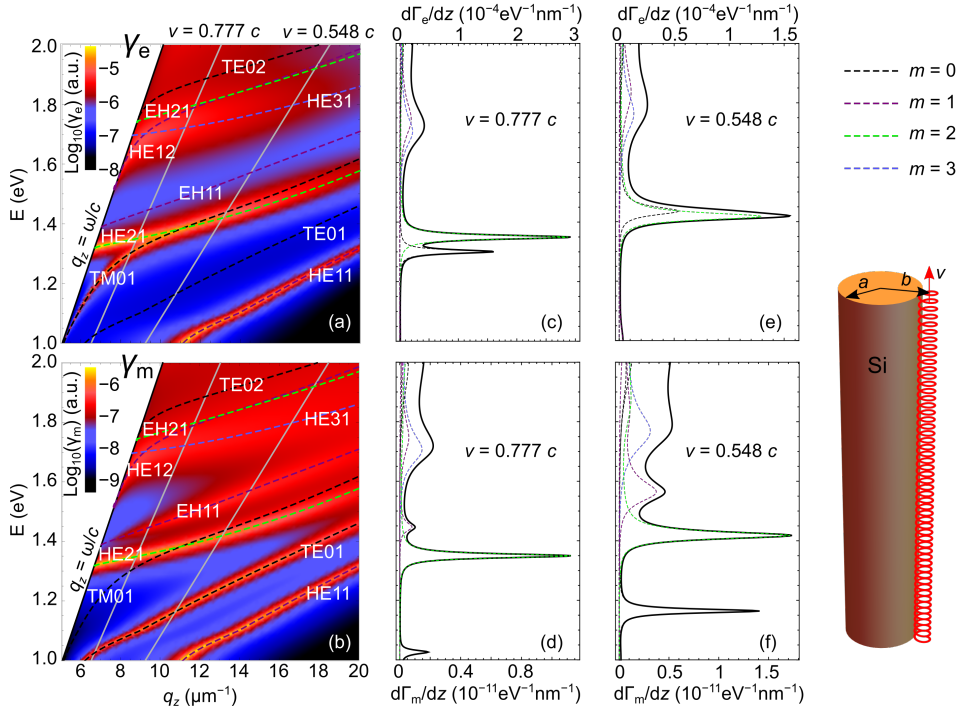


FIG. 3: EEL probability calculations for an electron beam moving parallel to the axis of an infinite silicon cylinder along the  $z$  direction (see the schematics) with speed  $v$ . The radius of the cylinder is  $a = 150$  nm and the beam distance from the center of the cylinder is  $b = 160$  nm. (a,b) Electric- and magnetic-current mediated ( $q_z, \omega$ )-dependent loss probabilities  $\gamma_e$  from Eq. (12) and  $\gamma_m$  from (13) in logarithmic color scale. Dashed lines overlaying the density plot correspond to dispersions of different azimuthal modes  $m$  from Eq. (14) (color coding shown in the legend). Solid gray lines show the wavevectors provided by the electron beam,  $q_z = \omega/v$  for velocities  $v = 0.777c$  (300-keV beam) and  $v = 0.548c$  (100-keV beam). (c,d) Loss probabilities per unit trajectory corresponding to the electric current component [Eq. (12)] and to the magnetic current component [Eq. (13)] calculated for a 300-keV beam (solid black line) and  $l = 100$ . The dashed lines show contributions of different azimuthal components  $m$  to the spectra. (e,f) the same as (c,d) but for a 100-keV beam. For plots (a,b) we considered only the first four azimuthal modes in the summation. The total probabilities in (c-f) were calculated with  $m = 0, 1, \dots, 6$ .

cylinder obtained as solutions of Eq. (14) for the different orders  $m$  denoting the modes' azimuthal symmetry. We consider only the first four azimuthal numbers  $m = \{0, 1, 2, 3\}$ , and as higher-order modes are much more damped, with these modes we are able to capture all the dominant spectral features. We can observe that some of the modes (denoted by using the standard notation from waveguide theory, see *e.g.* Refs.<sup>60,61</sup>) are visible only in the electrical contribution to the spectra,  $\gamma_e$  [Fig. 3(a)] or, *vice versa*, in the magnetic contribution,  $\gamma_m$  [Fig. 3(b)]. We can conclude that due to the symmetry of the EM field produced by the current components, transverse electric modes (TE01, TE01,...) are excitable only by the magnetic current. On the contrary, transverse magnetic modes (TM01, TM02,...) couple only to the electric current component.

From the  $(q_z, \omega)$ -dependent plots in Fig. 3(a,b) we can readily obtain the EEL spectra by setting  $q_z = \omega/v$  [see the gray lines in Fig. 3(a,b)], which corresponds to the wavevector provided by the electron moving along the

$z$  direction. In Fig. 3(c,d) we plot  $d\Gamma_{e,J_e}/dz$  [Eq. (12)] and  $d\Gamma_{m,J_m}/dz$  [Eq. (13)], respectively, evaluated for a 300-keV electron beam ( $v = 0.777c$ ). The total probabilities (solid black lines) are split into contributions of the different azimuthal modes  $m = \{0, 1, 2, 3\}$  denoted by the colored dashed lines. We observe that the hybrid HE21 mode produces the dominant spectral feature in both cases. On the other hand, the peak corresponding to the excitation of the TM01 mode is present only in the spectrum of Fig. 3(c), and the peak arising from the excitation of the TE01 mode appears only in Fig. 3(d). The hybrid EH11 is also dominantly excitable by the magnetic current, and has only a negligible contribution in the electric-current-mediated spectrum, as confirmed by evaluating the induced fields given in Appendix C.

By changing the acceleration voltage to 100 kV, we obtain the spectra in Fig. 3(e,f), where the same modes give rise to peaks at slightly different energies due to the change of the energy-momentum matching (higher  $q_z$  is provided at a fixed energy compared to the faster 300-

keV electron). Importantly, the standard electrical component of the EEL probability in geometries possessing translational invariance, such as in the current situation of the beam moving parallel to an infinite cylinder, can be related to the electrical part of the projected photonic local density of states (LDOS)<sup>62</sup>. An analogous proportionality holds between the magnetic-current-mediated loss and the magnetic part of the photonic LDOS. Hence, this relationship might be used in the context of the interaction of magnetic emitters with such structures. Our results are consistent with the findings in Ref.<sup>63</sup>, where the coupling of modes to differently oriented electric dipoles was linked to the excitation by electric/magnetic current components.

### C. Dichroic spectroscopy with vortex electron beams

Until now, we have considered a geometrical arrangements yielding zero or negligible dichroic signal, *i.e.*, no difference in VEB-EEL spectra obtained with a beam featuring positive OAM ( $l > 0$ ,  $\Gamma_{l+}$ ) and negative OAM ( $l < 0$ ,  $\Gamma_{l-}$ ). However, dichroism in VEB-EELS can emerge when the beam interacts with a chiral nanostructure or a chiral molecule. For an extended VEB, the main contribution to the dichroic signal is connected with the exchange of OAM<sup>47</sup>. However, in the following we prove that even within the approximation of a well-focused VEB with no OAM exchange, dichroic signal can arise.

For the demonstration purpose, we start with a simple model of a point-like dipolar object characterized by a combined isotropic polarizability including electric polarizability  $\alpha_{EE}$ , magnetic polarizability  $\alpha_{MM}$ , electromagnetic and magneto-electric polarizabilities  $\alpha_{EM}$  and  $\alpha_{ME} = -\alpha_{EM}$ , respectively. In such scenario, the EEL probability obtained with a focused electron vortex beam can be calculated as<sup>47</sup>

$$\Gamma = \frac{1}{\pi\hbar} \text{Im} [\mathbf{p} \cdot (\mathbf{E}_{\mathbf{J}_e}^*(\mathbf{r}_{\text{dip}}, \omega) + \mathbf{E}_{\mathbf{J}_m}^*(\mathbf{r}_{\text{dip}}, \omega)) + \mathbf{m} \cdot (\mathbf{B}_{\mathbf{J}_e}^*(\mathbf{r}_{\text{dip}}, \omega) + \mathbf{B}_{\mathbf{J}_m}^*(\mathbf{r}_{\text{dip}}, \omega))], \quad (15)$$

where we introduced the electric and magnetic fields produced due to the electric/magnetic current components  $\mathbf{E}_{\mathbf{J}_{e/m}}$  and  $\mathbf{B}_{\mathbf{J}_{e/m}}$ , respectively [see Eqs. (B2) and (B3) of Appendix B] evaluated at the particle position  $\mathbf{r}_{\text{dip}}$ . The induced electric and magnetic dipole moments are  $\mathbf{p} = \alpha_{EE}(\mathbf{E}_{\mathbf{J}_e} + \mathbf{E}_{\mathbf{J}_m}) + \alpha_{ME}(\mathbf{B}_{\mathbf{J}_e} + \mathbf{B}_{\mathbf{J}_m})$  and  $\mathbf{m} = \alpha_{MM}(\mathbf{B}_{\mathbf{J}_e} + \mathbf{B}_{\mathbf{J}_m}) + \alpha_{EM}(\mathbf{E}_{\mathbf{J}_e} + \mathbf{E}_{\mathbf{J}_m})$ , respectively, where the fields are again evaluated at  $(\mathbf{r}_{\text{dip}}, \omega)$ . Now, we can plug Eqs. (B2) and (B3) into Eq. (15) considering OAM  $+\hbar l$  and  $-\hbar l$ . Subtracting the probabilities then yields the dichroic signal:

$$\Gamma_{l+} - \Gamma_{l-} = \frac{-4|l|\mu_B\omega}{\pi\hbar e c^2} \text{Re}[\alpha_{EM}] [|\mathbf{E}_{\mathbf{J}_e}(\mathbf{r}_{\text{dip}}, \omega)|^2 + c^2 |\mathbf{B}_{\mathbf{J}_e}(\mathbf{r}_{\text{dip}}, \omega)|^2]. \quad (16)$$

Interestingly, the proportionality of the dichroic signal to  $-\text{Re}[\alpha_{EM}]$  holds also for optical circular dichroism (CD)<sup>64</sup>. However, compared to far-field optical spectroscopy with circularly-polarized light, the local excitation by a focused VEB makes it possible to probe chiral properties of nanostructures with high spatial resolution, which is manifested in the fast decay of the signal strength with increasing distance of the electron beam from the particle, as the EEL probability strongly depends on the field accompanying the VEBs. By further analyzing the dichroic VEB-EELS signal, we find that it stems from the *crossed* interaction between the electrically induced magnetic response and the magnetic current, and vice versa, contained in the terms  $\Gamma_{m, \mathbf{J}_e}$  and  $\Gamma_{e, \mathbf{J}_m}$ , respectively.

Now we demonstrate the emergence of the dichroic signal when an extended chirally-arranged nanostructure is probed by a VEB. We adopt a similar geometry as the one studied in Ref.<sup>65</sup>, and perform the numerical modeling. We consider two vertically displaced cylindrical rods rotated by 90° and stacked at their corners as shown in the schematics of Fig. 4. The overall response of the structure in such an arrangement can be described with an effective electric and electro-magnetic polarizability<sup>65</sup> and thus, according to the preceding analysis, we should expect the emergence of dichroism also in the VEB-EEL spectra. However, the finite spatial extent of the structure, as well as the overlap of different electro-magnetic modes excited in the silicon rods, might produce a non-trivial spatial dependence of the dichroic signal.

We set the length of each rod,  $L = 800$  nm, radius  $a = 80$  nm and vertical spacing between the rods  $g = 30$  nm as shown in the inset of Fig. 4(a). We calculate EEL spectra for an excitation by a VEB with energy 100 keV and OAM  $l = \pm 100$  at different beam positions. The spectra in Fig. 4(a) are obtained for the beam placed at the corner between the rods, 10 nm from their boundaries, whereas in Fig. 4(b) the beam is located at 10 nm from the tip of one of the rods (see the corresponding insets). We split the relevant spectral components as in Eqs. (6) and (7): the purely electric loss probability term  $\Gamma_{e, \mathbf{J}_e}$  (solid red line), and the *crossed* electric-magnetic terms  $\Gamma_{e, \mathbf{J}_m}$  (dashed red line) and  $\Gamma_{m, \mathbf{J}_e}$  (dashed blue line). We do not plot the purely magnetic term  $\Gamma_{m, \mathbf{J}_m}$ , which is several orders of magnitude weaker.

The modes of a finite silicon cylinder can be understood as standing waves along the long axis of the cylinder, formed by the different modes of an infinite cylinder<sup>55,66</sup>, as shown in Sec. III B. The first dominant peak in  $\Gamma_{e, \mathbf{J}_e}$  close to 0.8 eV in Fig. 4(a,b) originates mostly from the bonding arrangement of two dipolar modes along both rods [as can be noted also in the energy-filtered map in Fig. 4(c)] with TM01 transverse modal profile. This mode couples well in this geometry to the EM field associated with the electric current component as found from the analysis of the induced field. The second-order mode with TM01 modal profile appears around 1.3 eV [the corresponding peak is clearly visible

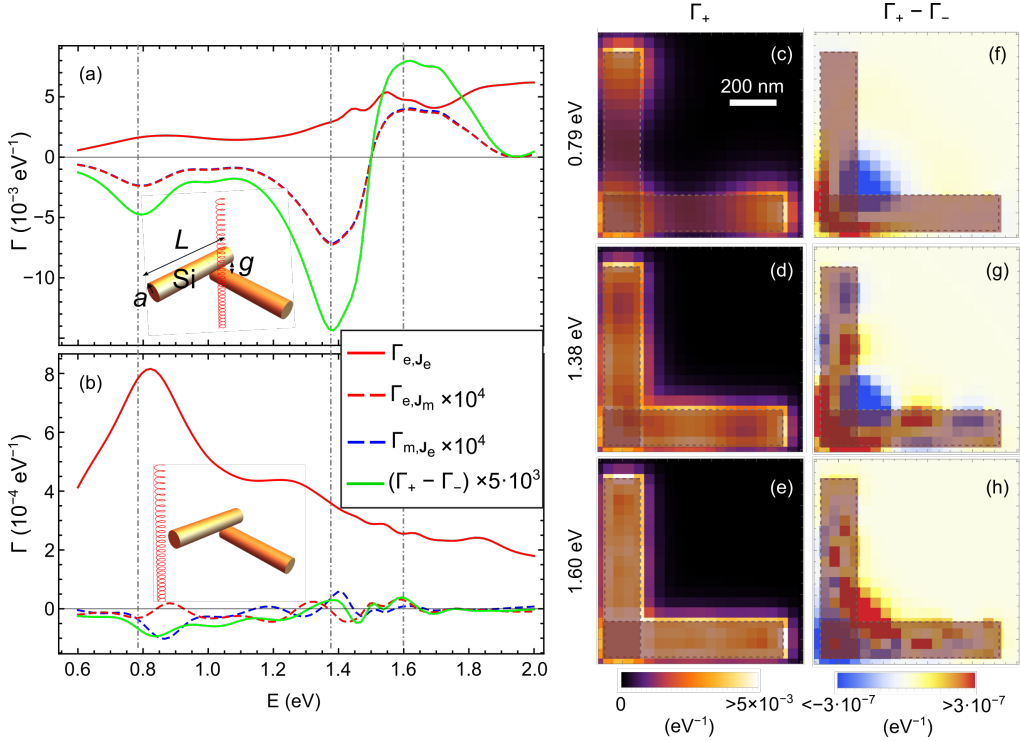


FIG. 4: (a,b) VEB-EEL spectra calculated for chirally-arranged silicon rods with parameters  $a = 80 \text{ nm}$ ,  $L = 800 \text{ nm}$ ,  $g = 30 \text{ nm}$  [see the inset of (a)]. The dielectric response of silicon is taken from Ref. <sup>49</sup>. We consider the excitation by a 100 keV VEB with  $l = +100$  and split the spectral contributions according to Eqs. (6) and (7):  $\Gamma_{e,J_e}$  (solid red line),  $\Gamma_{e,J_m} \times 10^4$  (dashed red line), and  $\Gamma_{m,J_e}$  (dashed blue line). We omit the  $\Gamma_{m,J_m}$  term. The green line shows VEB-EEL dichroism obtained as a difference between spectra calculated for  $l = +100$  and  $l = -100$ . In (a) the beam is positioned according to the inset 10 nm from the surface of the rods, whereas in (b) the beam is placed 10 nm from the tip of one of the rods as depicted. (c-e) Energy-filtered maps of the total EEL for  $l = +100$ , and (f-h) the dichroic signal at energies marked on the left of each row. The selected energies correspond to positions of the peaks in the dichroic signal in (a). The spatial scaling is the same in all maps and the boundaries of the cylinders are plotted by dashed gray lines while their cross sections are shown as semi-transparent rectangles.

in Fig. 4(b)], but it significantly overlaps with an admixture of higher-order electric and magnetic modes from higher energies. Hence, due to this overlap, the energy-filtered maps at energies 1.38 eV [Fig. 4(d)] and also at 1.6 eV [Fig. 4(e)] show nearly homogeneous intensity for all beam positions close to the rod surfaces.

Importantly, there is a small difference between the spectra  $\Gamma_+$  and  $\Gamma_-$ , which we plot with solid green lines in Fig. 4(a,b). The dichroism in EEL emerges from the *crossed* loss terms  $\Gamma_{e,J_m}$  and  $\Gamma_{m,J_e}$  [dashed lines in Fig. 4(a,b)]. As we can observe in the energy-filtered maps of  $(\Gamma_+ - \Gamma_-)$  [Fig. 4(f-h)], the strongest dichroic response arises for the beam close to the stacking point of the rods, where the strongest interference and the phase difference between the fields induced at each of the rods appears. Similar behavior was predicted in a recent work<sup>67</sup>. The dichroic VEB-EEL spectra also flip sign depending on the structure of the local phase and the nature of the induced field along the  $z$  axis. The sign change of the dichroic signal appears in the region between 1.4 eV and 1.6 eV, where hybridized modes with TE polarization, *i.e.* coupled magnetic dipoles and higher-order modes polarized along the long axes of the

rods, can be excited. These modes couple preferentially to the EM field of the magnetic current component, which changes its sign depending on  $l$  [see Eqs. S1]. Hence, the sign of the dichroic signal might in this case reflect whether a particular mode preferentially couples with either the electric or the magnetic current component of the VEB. However, we note that the interpretation of spatially-resolved dichroic VEB-EELS in a general case can be rather involved, and requires further theoretical analysis.

Although the dichroic signal is three to four orders of magnitude weaker than the overall spectra, experimental development might make it detectable<sup>68</sup>. We note that our approach assuming an infinitely focused VEB presumably underestimates the intensity of the dichroic signal. By taking into account an overlap of a realistic beam profile with the electromagnetic field in the structure (*e.g.*, as in Refs. <sup>45,47</sup>), one might expect a higher contribution of the dichroic signal to the overall loss probability, with a qualitatively similar spatial dependence.

#### IV. CONCLUSIONS

We set a classical theoretical framework suitable for a qualitative modeling of vortex electron energy loss spectroscopy at optical frequencies, in the limit of a perfectly-focused vortex beam. We revealed that spatially-resolved EELS acquired with electron vortices could be a powerful technique for a detailed characterization of the optical response of complex nanostructures, which we demonstrated on several examples: spherical particles and cylindrical wires made of silicon. In particular, we showed how to interpret EEL spectra based on field symmetry considerations and demonstrated that we could distinguish modes of electric or magnetic nature emerging in the dielectric nanoparticles by varying electron's velocity or OAM. We also proved the emergence of dichroism in electron spectra recorded with vortex electrons, which could establish VEB-EELS as a unique technique to characterize chirality at the nanoscale.

#### Acknowledgments

Research of A.K., R.H. and J.A. was supported by the Spanish Ministry of Economy, Industry and Competitiveness (project PID2019-107432GB-I00, project MDM-2016-0618 of the Maria de Maetzu Units of Excellence Programme). M.K.S. acknowledges support from the Macquarie University Research Fellowship Scheme (MQRF0001036). A.K. was supported by the ESF under the project CZ.02.2.69/0.0/0.0/20\_079/0017436.

#### Appendix A: Inelastic electron transition probability: quantum description of the beam

##### 1. General formulation

The wavefunction of a vortex electron,  $\psi_l$ , can be described in the non-relativistic approximation (for discussion of the relativistic solutions, see Refs.<sup>69,70</sup>) as a solution of the Schrödinger equation for a free-space moving electron with a non-vanishing angular momentum  $l\hbar$ . In cylindrical coordinates  $(R, \phi, z)$ , one of the simplest solutions takes the form of a Bessel beam<sup>28-30</sup>

$$\psi(R, \phi, z) = \frac{1}{\sqrt{L}} e^{iq_z z} \psi_{\perp}, \quad (\text{A1})$$

where  $Q$  and  $q_z = m_e v / \hbar$  are the radial and perpendicular wavevectors of the electron moving along the  $z$  axis, respectively, and  $\psi_{\perp} = 1/\sqrt{A} e^{il\phi} J_l(QR)$ .  $A$  stands for a normalization area and  $L$  for a normalization length. The Bessel function of order  $l$ ,  $J_l(QR)$ , governs the radial shape of the beam whereas the helical form of the wavefront is captured through the exponential term  $e^{il\phi}$ , which determines the phase variation in the transverse plane.

We now express the rate of transition from a well-defined initial state  $\psi_i$  to final states  $\psi_f$  (following the formalism from Ref.<sup>47</sup>) as

$$\begin{aligned} \frac{d\Gamma_{fi}(\omega)}{dt} = & \frac{2\hbar e^2}{\omega^2 m_e^2} \int d^3\mathbf{r} d^3\mathbf{r}' \psi_f(\mathbf{r}) \psi_f^*(\mathbf{r}') \nabla [\psi_i^*(\mathbf{r})] \cdot \\ & \cdot \text{Im} [\hat{\mathbf{G}}(\mathbf{r}, \mathbf{r}', \omega)] \cdot \nabla [\psi_i(\mathbf{r}')] \delta(\epsilon_f - \epsilon_i + \omega), \end{aligned} \quad (\text{A2})$$

where  $\hbar\epsilon_{f/i}$  is the final/initial electron energy, and  $\hat{\mathbf{G}}$  is the Green's tensor describing electromagnetic response of the probed structure. For the comparison with the (semi-)classical results presented in the main text, we consider the states  $\psi_i = e^{iq_{z,i}z} \psi_{\perp,i} / \sqrt{L}$  and  $\psi_f = e^{iq_{z,f}z} \psi_{\perp,f} / \sqrt{L}$  with initial and final longitudinal wavevectors  $q_{z,i}$  and  $q_{z,f}$ , respectively, and we set OAM  $l_i = l_f = l$ , *i.e.* we are interested in transition between the vortex states characterized by identical OAM. We further consider  $\psi_{\perp,f} = e^{il\phi} J_l(Q_f R) / \sqrt{A}$  with a set of possible transverse wavevectors  $Q_f$  and a well-defined initial transverse wavefunction  $\psi_{\perp,i} \approx 1/(Q_{c,i}\sqrt{\pi}) \int_0^{Q_{c,i}} Q_i dQ_i e^{il\phi} J_l(Q_i R)$  where  $Q_{c,i}$  is an initial wavevector cutoff.

The loss probability per electron then becomes

$$\Gamma(\omega) = \frac{L}{v} \sum_f \frac{d\Gamma_{fi}(\omega)}{dt}, \quad (\text{A3})$$

where we sum over the final states, we integrate over the longitudinal wavevector  $q_{z,f}$ :  $\sum_f \rightarrow L/(2\pi) \int dq_{z,f} \sum_{f_{\perp}}$ , and transverse wavevectors  $\sum_{f_{\perp}} = A/(2\pi)^2 \int_0^{Q_c} Q_f dQ_f \int_0^{2\pi} d\phi_f = A/(2\pi) \int_0^{Q_c} Q_f dQ_f$ , where we used the symmetry of the expression under the integral and defined the cutoff transverse final wavevector  $Q_c$ .

We also rewrite the spatial integrals over  $\mathbf{r}$  and  $\mathbf{r}'$  in cylindrical coordinates, which after collecting all  $z$ - and  $z'$ -dependent exponentials from the  $\psi$ 's [see Eq. (A1)], using the identity  $\int dq_{z,f} \exp[i(q_{z,f} - q_{z,i})(z - z')] \delta(\epsilon_f - \epsilon_i + \omega) = 1/v \exp[-i\omega(z - z')/v]$ , and defining

$$\hat{\mathcal{G}}(\mathbf{R}, \mathbf{R}') = \int dz dz' e^{-i\omega(z - z')/v} \text{Im}[\hat{\mathbf{G}}(\mathbf{r}, \mathbf{r}', \omega)], \quad (\text{A4})$$

becomes

$$\begin{aligned} \Gamma(\omega) = & \frac{e^2}{2\pi^3 \hbar \omega^2 Q_{c,i}^2} \int_0^{Q_c} Q_f dQ_f \int d\mathbf{R} d\mathbf{R}' \\ & \times J_l(Q_f R) J_l(Q_f R') f(R) f(R') \left[ \mathbf{V}^*(R) \cdot \hat{\mathcal{G}} \cdot \mathbf{V}(R') \right], \end{aligned} \quad (\text{A5})$$

where we defined  $f(R) = \int_0^{Q_{c,i}} Q_i dQ_i J_l(Q_i R)$ . Vector fields  $\mathbf{V}$  describe the gradient of electron's wavefunctions [Eq. (A2)], and are given by

$$\mathbf{V}(R, \phi) = \mathbf{e}_z + \frac{\mathbf{e}_{\phi} l}{R q_{z,i}} - \mathbf{e}_R i \frac{f'(R)}{f(R)}, \quad (\text{A6})$$

which stems from  $\nabla[\psi_i^*(\mathbf{r})] = i q_{z,i} \mathbf{V}^*(R, \phi) \psi_i^*(\mathbf{r})$ .

If all electrons are collected by the detector, we have  $Q_c \rightarrow \infty$  and we can use the identity  $\int_0^\infty x dx J_l(xR) J_l(xR') = \delta(R - R')/R'$  to perform the integral over the final transverse wavevectors to get

$$\begin{aligned} \Gamma(\omega) &= \frac{e^2}{2\pi^3 \hbar \omega^2 Q_{c,i}^2} \int_0^\infty R dR f^2(R) \\ &\times \int_0^{2\pi} d\phi \int_0^{2\pi} d\phi' \left[ \mathbf{V}^*(R, \phi) \cdot \hat{\mathbf{G}}(R, R, \phi, \phi') \cdot \mathbf{V}(R, \phi') \right]. \end{aligned} \quad (\text{A7})$$

Note that  $f^2(R)$  will be strongly peaked around an effective initial VEB radius  $R_{0,l}$  given by the initial cutoff value. Therefore if we consider  $\hat{\mathbf{G}}$  slowly varying around  $R_{0,l}$ , we can roughly approximate the integral over  $R$  by  $\int_0^\infty R dR f^2(R) = Q_{c,i}^2/2$  to obtain

$$\begin{aligned} \Gamma(\omega) &\approx \frac{e^2}{4\pi^3 \hbar \omega^2} \int_0^{2\pi} d\phi \int_0^{2\pi} d\phi' \left[ \mathbf{W}^*(R_{0,l}, \phi) \cdot \right. \\ &\quad \left. \cdot \hat{\mathbf{G}}(R_{0,l}, R_{0,l}, \phi, \phi') \cdot \mathbf{W}(R_{0,l}, \phi') \right], \end{aligned} \quad (\text{A8})$$

where we disregarded the radial component of  $\mathbf{V}$  as it is 0 at  $R_{0,l}$  (or much smaller than the  $\phi$  component close to  $R_{0,l}$ ) yielding

$$\mathbf{W}(R, \phi) = \mathbf{e}_z + \frac{\mathbf{e}_\phi l}{R q_{z,i}}. \quad (\text{A9})$$

Importantly, the different projections of the Green's tensor due to products with the vector  $\mathbf{W}$  can be interpreted in connection with the classical formalism, as losses experienced by different components of the electric current due to the fields emerging in the excitation by all these current components. We further explore these contributions in the following section on a canonical example of the excitation of a point-like dipolar particle.

## 2. Loss probability for a point-like dipolar particle

Here we present the Green's tensor necessary to calculate the loss probability in the presence of a point-like particle situated at  $\mathbf{r}_p = (\mathbf{R}_p, z_p)$ , electrically and magnetically polarizable in the  $z$  direction, and characterized by the electric polarizability tensor  $\hat{\alpha}_{EE} = \alpha_{EE}(\mathbf{0}, \mathbf{0}, \mathbf{e}_z)$  and magnetic polarizability tensor  $\hat{\alpha}_{MM} = \alpha_{MM}(\mathbf{0}, \mathbf{0}, \mathbf{e}_z)$ , respectively. The Green's tensor is then

$$\begin{aligned} \hat{\mathbf{G}}(\mathbf{r}, \mathbf{r}', \omega) &= \hat{\mathbf{G}}_{EE}(\mathbf{r}_p - \mathbf{r}') \cdot \hat{\alpha}_{EE} \cdot \hat{\mathbf{G}}_{EE}(\mathbf{r} - \mathbf{r}_p) \\ &+ \hat{\mathbf{G}}_{EM}(\mathbf{r}_p - \mathbf{r}') \cdot \hat{\alpha}_{MM} \cdot \hat{\mathbf{G}}_{ME}(\mathbf{r} - \mathbf{r}_p) \end{aligned} \quad (\text{A10})$$

with  $\hat{\mathbf{G}}_{EE}(\mathbf{r}) = \hat{\mathbf{G}}_{MM}(\mathbf{r}) = (k^2 \hat{\mathbf{I}} + \nabla \otimes \nabla) e^{ikr} / (4\pi \varepsilon_0 r)$  and  $\hat{\mathbf{G}}_{EM}(\mathbf{r}) = -\hat{\mathbf{G}}_{ME}(\mathbf{r}) = -\nabla \times \hat{\mathbf{G}}_{EE}(\mathbf{r}) / (ikc)$ , where  $k = \omega/c$  with the speed of light  $c$ ,  $\varepsilon_0$  is the vacuum permittivity and  $\otimes$  denotes tensor product.

The integrals over  $z$  (and  $z'$ ) involved in  $\hat{\mathbf{G}}$  are analytical:

$$\begin{aligned} \hat{\mathbf{G}}_{EE}^{\text{int}} &= \int dz e^{-i\omega z/v} \hat{\mathbf{G}}_{EE}(\mathbf{r} - \mathbf{r}_p) \\ &= \frac{2}{4\pi \varepsilon_0} (k^2 \hat{\mathbf{I}} + \nabla_{\mathbf{r}_p} \otimes \nabla_{\mathbf{r}_p}) e^{-i\omega z_p/v} K_0 \left( \frac{\omega |\mathbf{R} - \mathbf{R}_p|^2}{v \gamma_L} \right), \end{aligned} \quad (\text{A11})$$

and

$$\hat{\mathbf{G}}_{EM}^{\text{int}} = \int dz e^{-i\omega z/v} \hat{\mathbf{G}}_{EM}(\mathbf{r} - \mathbf{r}_p) = \frac{1}{ikc} \nabla_{\mathbf{r}_p} \times \hat{\mathbf{G}}_{EE}^{\text{int}}, \quad (\text{A12})$$

which we use to obtain

$$\begin{aligned} \hat{\mathbf{G}}(\mathbf{R}, \mathbf{R}') &= \hat{\mathbf{G}}_{EE}^{\text{int}}(\mathbf{R}_p - \mathbf{R}') \cdot \text{Im}[\hat{\alpha}_{EE}] \cdot \hat{\mathbf{G}}_{EE}^{\text{int}}(\mathbf{R} - \mathbf{R}_p) \\ &\quad - \hat{\mathbf{G}}_{EM}^{\text{int}}(\mathbf{R}_p - \mathbf{R}') \cdot \text{Im}[\hat{\alpha}_{MM}] \cdot \hat{\mathbf{G}}_{EM}^{\text{int}}(\mathbf{R} - \mathbf{R}_p). \end{aligned} \quad (\text{A13})$$

For final states with  $l = 0$ , we have  $R_{0,0} = 0$  and the loss probability reduces to

$$\begin{aligned} \Gamma_{l=0}(\omega) &\approx \frac{e^2}{4\pi^3 \hbar \omega^2} \int_0^{2\pi} d\phi \int_0^{2\pi} d\phi' \hat{\mathcal{G}}_{zz'}(0, 0, \phi, \phi') \\ &= \frac{e^2 \omega^2}{16\pi^5 \varepsilon_0^2 \hbar v^4 \gamma_L^4} \text{Im}[\alpha_{EE}] \left[ \int_0^{2\pi} d\phi K_0 \left( \frac{\omega R_p}{v \gamma_L} \right) \right]^2 \\ &= \frac{e^2 \omega^2}{4\pi^3 \varepsilon_0^2 \hbar v^4 \gamma_L^4} \text{Im}[\alpha_{EE}] K_0^2 \left( \frac{\omega R_p}{v \gamma_L} \right) \end{aligned} \quad (\text{A14})$$

Importantly, the above result coincides with the classical limit with a well-focused beam at the origin. We can see that in this special case, the beam interacts only with the electric dipole and the interaction is mediated via the electric-electric part of the Green's tensor, in particular its  $zz'$  component. The magnetic dipole could be probed only if polarization in the transverse plane was allowed.

Now we evaluate the loss probability for small  $|l| \neq 0$ . We find that the resulting energy loss can be expressed as

$$\Gamma(\omega) = \Gamma_{l=0}(\omega) + \Gamma_{\text{VEB}}(\omega), \quad (\text{A15})$$

where

$$\begin{aligned} \Gamma_{\text{VEB}}(\omega) &\approx \frac{-e^2 l^2}{4\pi^3 \hbar \omega^2 c^2 R_{0,l}^2 q_{z,i}^2} \\ &\times \int_0^{2\pi} d\phi \int_0^{2\pi} d\phi' \hat{\mathcal{G}}_{\phi\phi'}(R_{0,l}, R_{0,l}, \phi, \phi') \\ &= \frac{e^2 l^2 \omega^2}{16\pi^5 \varepsilon_0^2 \hbar v^2 c^4 \gamma_L^2 R_{0,l}^2 q_{z,i}^2} \text{Im}[\alpha_{MM}] \\ &\left[ \int_0^{2\pi} d\phi \frac{(R_{0,l} - R_p \cos \phi)}{\sqrt{R_{0,l}^2 + R_p^2 - 2R_{0,l} R_p \cos \phi}} \right. \\ &\quad \left. \times K_1 \left( \frac{\omega \sqrt{R_{0,l}^2 + R_p^2 - 2R_{0,l} R_p \cos \phi}}{v \gamma_L} \right) \right]^2 \end{aligned}$$

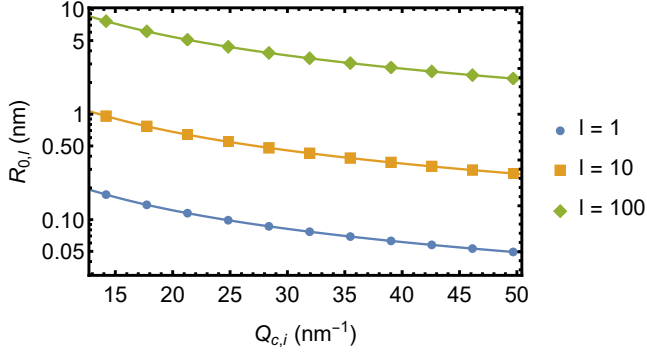


FIG. 5: Effective beam radius as a function of the initial transverse wavevector cutoff calculated for OAM of  $\hbar$ ,  $10\hbar$  and  $100\hbar$ . We find that numerically-calculated data (points) approximately follow  $1/Q_{c,i}$  dependence with the corresponding fits plotted as solid lines. In practice, there is a finite achievable radius given by the maximal possible convergence angle.

$$= \frac{e^2 l^2 \omega^2}{4\pi^3 \varepsilon_0^2 \hbar v^2 c^4 \gamma_L^2 R_{0,l}^2 q_{z,i}^2} \text{Im}[\alpha_{\text{MM}}] \\ \times \begin{cases} I_1^2 \left( \frac{\omega R_{0,l}}{v \gamma_L} \right) K_0^2 \left( \frac{\omega R_p}{v \gamma_L} \right) & \text{for } R_{0,l} \leq R_p, \\ I_1^2 \left( \frac{\omega R_p}{v \gamma_L} \right) K_0^2 \left( \frac{\omega R_{0,l}}{v \gamma_L} \right) & \text{for } R_{0,l} > R_p, \end{cases} \quad (\text{A16})$$

and where we evaluated the integrals following Ref. <sup>47</sup>. We note that for a well-focused VEB with  $\omega R_{0,l}/(v \gamma_L) \rightarrow 0$ , and thus using  $I_1(x) \sim x/2$  for small arguments, we obtain

$$\Gamma_{\text{VEB}}(\omega) \approx \frac{e^2 l^2 \omega^4}{16\pi^3 \varepsilon_0^2 \hbar v^4 c^4 \gamma_L^4 q_{z,i}^2} \text{Im}[\alpha_{\text{MM}}] K_0^2 \left( \frac{\omega R_p}{v \gamma_L} \right), \quad (\text{A17})$$

which is very accurate for  $R_{0,l} \lesssim 10$  nm at optical frequencies and for typical acceleration voltages. Such effective radii are achievable even for relatively large  $l$  ( $\sim 100$ ) as demonstrated in Fig. 5.

Importantly, considering typical amplitudes of polarizability components ( $\text{Im}[\alpha_{\text{MM}}] \sim c^2 \text{Im}[\alpha_{\text{EE}}]$ ), we can see that the contribution to the loss probability due to the interaction of the electric field with the electric current in the  $z$  direction ( $\Gamma_{l=0}$ ) will be dominant as  $\Gamma_{\text{VEB}}$  is  $[2q_{z,i}c/(l\omega)]^2 \sim 10^{11}$  smaller for  $l = 1$  excitations in the optical range, and typical acceleration voltages. This rather small contribution can be translated as loss experienced by an equivalent magnetic current due to the excited magnetic field. We note that for small particles exhibiting dichroic response characterized by the corresponding polarizability  $\alpha_{\text{EM}}$ , we will also have *crossed* terms coming from the electric-magnetic interaction, with the corresponding loss probability  $\sim 2q_{z,i}c/(l\omega) \sim 10^5 - 10^6$  smaller than the usual electric-electric loss. These numbers can be improved by using VEBs with larger OAM.

## Appendix B: Equivalent electric and magnetic current components and corresponding electromagnetic field

In the limiting case of a point-like particle placed beyond the effective beam radius studied in the previous section, and using symmetries in Green's tensor components for electric/magnetic excitation (invariance of Maxwell's equations), we can find that the approximate electric current (neglecting its radial component)  $\mathbf{J}_e(R) = -e\mathbf{W}(R)e^{i\omega z/v}$  can be equivalently replaced by two sources  $\mathbf{J}_e(R) = -e e^{i\omega z/v} \mathbf{e}_z$  and

$$\mathbf{J}_m \approx \frac{ie\omega}{2q_{z,i}} e^{i\omega z/v} \mathbf{e}_z = \frac{il\omega \mu_B}{v} e^{i\omega z/v} \mathbf{e}_z. \quad (\text{B1})$$

However, we note that especially for larger  $l$  or for probed structures with dimensions comparable to the vortex focus, the loss probability calculated using this model can differ both qualitatively and quantitatively from the rigorous approach, *i.e.* using the overlap integral in Eq. (A5) within the quantum-mechanical description of the VEBs. We also note that an alternative magnetic current deduced from an effective spiralling electric current, as presented in Ref. <sup>46</sup>, is expressed as  $\mathbf{J}_m = 2ile\hbar c^2/(m_e v R_{0,l}^2 \omega) e^{i\omega z/v} \mathbf{e}_z$ , which involves an additional factor  $4c^2/(R_{0,l}^2 \omega^2)$  in their expression, as compared to Eq. (B1). The expression in Ref. <sup>[46]</sup> provides values 1–4 orders of magnitude larger than those obtained with our formulation in the optical range and for reasonable beam radius.

The electromagnetic field produced due to these current components can be expressed as

$$\mathbf{E}_{\mathbf{J}_e}(\mathbf{r}, \omega) = \frac{e\omega e^{i\omega z}}{2\pi\varepsilon_0\gamma_L v^2} \left[ -K_1 \left( \frac{\omega R}{v\gamma_L} \right) \mathbf{e}_R + \frac{i}{\gamma_L} K_0 \left( \frac{\omega R}{v\gamma_L} \right) \mathbf{e}_z \right], \quad (\text{B2a})$$

$$\mathbf{B}_{\mathbf{J}_e}(\mathbf{r}, \omega) = \frac{e\omega e^{i\omega z}}{2\pi\varepsilon_0\gamma_L v c^2} \left[ -K_1 \left( \frac{\omega R}{v\gamma_L} \right) \mathbf{e}_\phi \right], \quad (\text{B2b})$$

for the electric part of the current (placed at the origin), whereas the field produced by the magnetic current can be simply obtained by applying the transformation in Eq. (3) on Eqs. (B2):

$$\mathbf{E}_{\mathbf{J}_m}(\mathbf{r}, \omega) = \frac{i\mu_B l \omega^2 e^{i\omega z}}{2\pi\varepsilon_0\gamma_L v^3 c^2} \left[ -K_1 \left( \frac{\omega R}{v\gamma_L} \right) \mathbf{e}_R + \frac{i}{\gamma_L} K_0 \left( \frac{\omega R}{v\gamma_L} \right) \mathbf{e}_z \right], \quad (\text{B3a})$$

$$\mathbf{E}_{\mathbf{J}_m}(\mathbf{r}, \omega) = \frac{-i\mu_B l \omega^2 e^{i\omega z}}{2\pi\varepsilon_0\gamma_L v^2 c^2} \left[ -K_1 \left( \frac{\omega R}{v\gamma_L} \right) \mathbf{e}_\phi \right]. \quad (\text{B3b})$$

### Appendix C: Numerical calculations of (VEB-)EELS in Comsol Multiphysics

We utilize the **Radio Frequency** toolbox of **Comsol Multiphysics** software where we solve the wave equation for the total electric and magnetic field in the frequency domain with electric and magnetic current sources. We perform the calculations in a 3D simulation domain in the Cartesian coordinate system ( $x, y, z$ ). The simulation domain includes the nanostructure characterized by a dielectric response  $\varepsilon$ , a straight line representing the electron's trajectory, a simulation domain (typically a block) surrounding the nanostructure characterized by  $\varepsilon = 1$  and **Perfectly Matched Layers** (PML) with Cartesian symmetry that help to attenuate the electric field at the boundaries of the simulation domain and prevent unphysical field reflections from the boundaries.

We apply the **Free Tetrahedral** mesh with refined elements in areas of high field concentration and gradients, typically close to the electron's trajectory and nanostructures. We allow for an increase of the size of the mesh elements towards outer boundaries of the simulation domain. The area of PML is meshed by 5-10 **Swept** layers. The maximal allowed elements' dimensions depend on the simulated energy region and thus on the typical wavelengths involved. We typically use fractions of the typical wavelength for the largest elements.

The electric current density component assigned to either conventional or vortex electron beam is implemented as line **Edge Current**, specified by Eq. (1), whereas the magnetic current is given by line **Magnetic Current** as expressed in Eq. (2). The (VEB)-EEL probability is evaluated from 3D calculations according to Eq. (6) and Eq. (7) directly with this software using an **Edge Probe**, **Integral** along the electron's trajectory between the boundaries at  $z_{\min}$  and  $z_{\max}$ .

All simulations are performed twice: with  $\varepsilon(\mathbf{r}, \omega)$  corresponding to the probed structure and then with  $\varepsilon(\mathbf{r}, \omega) = 1$  everywhere, so that only the field of the electron is present, preserving the same discretization of the geometrical domains. Afterwards, the loss probability obtained from these two calculations is subtracted to obtain only the contribution coming from the induced field arising from the interaction of the electron beam with the nanostructure and to correct for the finite length of the electron's trajectory and non-zero values of the fast electron's field at the boundaries of the simulation domain<sup>5,71,72</sup>.

### Appendix D: Electron interacting with a dielectric cylinder

We adapt the expressions from Ref.<sup>59</sup> for the electromagnetic field expressed in cylindrical coordinates  $(R, \phi, z)$  for an electron beam moving in vacuum, parallel to an infinite dielectric cylinder along the  $z$  axis. The cylinder has a radius  $a$  and the electron beam is positioned at radial distance  $b > a$  from the center of the

cylinder.

The electric and magnetic field components, produced by the fast electron moving in vacuum, in cylindrical coordinates, and Fourier-transformed in the  $q_z$  space are:

$$\begin{aligned} E_{\text{el},z}(R, \phi, q_z, \omega) &= \frac{i\omega e\delta(\omega/v - q_z)}{v^2\varepsilon_0\gamma_L^2} \sum_{m=-\infty}^{\infty} [K_m(R\Omega) \\ &\quad \times I_m(b\Omega)H(R-b) + K_m(b\Omega)I_m(R\Omega)H(b-R)] e^{im\phi}, \\ E_{\text{el},R}(R, \phi, q_z, \omega) &= \frac{\Omega e\delta(\omega/v - q_z)}{v\varepsilon_0} \sum_{m=-\infty}^{\infty} [K'_m(a\Omega) \\ &\quad \times I_m(b\Omega)H(R-b) + K_m(b\Omega)I'_m(R\Omega)H(b-R)] e^{im\phi}, \\ E_{\text{el},\phi}(R, \phi, q_z, \omega) &= \frac{i\omega e\delta(\omega/v - q_z)}{v\varepsilon_0} \sum_{m=-\infty}^{\infty} \frac{m}{R} [K_m(R\Omega) \\ &\quad \times I_m(b\Omega)H(R-b) + K_m(b\Omega)I_m(R\Omega)H(b-R)] e^{im\phi}, \\ H_{\text{el},z}(R, \phi, q_z, \omega) &= 0, \\ H_{\text{el},R}(R, \phi, q_z, \omega) &= -ie\delta(\omega/v - q_z) \sum_{m=-\infty}^{\infty} [K_m(R\Omega) \\ &\quad \times I_m(b\Omega)H(R-b) + K_m(b\Omega)I_m(R\Omega)H(b-R)] e^{im\phi}, \\ H_{\text{el},\phi}(R, \phi, q_z, \omega) &= \Omega e\delta(\omega/v - q_z) \sum_{m=-\infty}^{\infty} [K'_m(R\Omega) \\ &\quad \times I_m(b\Omega)H(R-b) + K_m(b\Omega)I'_m(R\Omega)H(b-R)] e^{im\phi}, \end{aligned}$$

where  $I_m(x)$  and  $K_m(x)$  are the modified Bessel functions of the first and the second kind, respectively, of order  $m$ , and  $H(x)$  is the Heaviside step function. We also defined  $\Omega = \omega/v\sqrt{1-v^2/c^2}$ . The components of the induced electric and magnetic field inside the cylinder ( $R < a$ ) characterized by a dielectric function  $\varepsilon$  are:

$$\begin{aligned} E_{\text{in},z}(R, \phi, q_z, \omega) &= \sum_{m=-\infty}^{\infty} -\kappa_i^2 a_{\text{e},m} I_m(\kappa_i R) e^{im\phi}, \\ E_{\text{in}R}(R, \phi, q_z, \omega) &= \sum_{m=-\infty}^{\infty} [iq_z \kappa_i a_{\text{e},m} I'_m(\kappa_i R) \\ &\quad - \frac{\omega\mu_0 m}{R} c_{\text{e},m} I_m(\kappa_i R)] e^{im\phi}, \\ E_{\text{in},\phi}(R, \phi, q_z, \omega) &= \sum_{m=-\infty}^{\infty} \left[ -\frac{mq_z}{R} a_{\text{e},m} I_m(\kappa_i R) \right. \\ &\quad \left. - i\omega\mu_0\kappa_i c_{\text{e},m} I'_m(\kappa_i R) \right] e^{im\phi}, \\ H_{\text{in},z}(R, \phi, q_z, \omega) &= \sum_{m=-\infty}^{\infty} -\kappa_i^2 c_{\text{e},m} I_m(\kappa_i R) e^{im\phi}, \\ H_{\text{in},R}(R, \phi, q_z, \omega) &= \sum_{m=-\infty}^{\infty} \left[ \frac{m\omega\varepsilon\varepsilon_0}{R} a_{\text{e},m} I_m(\kappa_i R) \right. \\ &\quad \left. + iq_z \kappa_i c_{\text{e},m} I'_m(\kappa_i R) \right] e^{im\phi}, \\ H_{\text{in},\phi}(R, \phi, q_z, \omega) &= \sum_{m=-\infty}^{\infty} [i\omega\varepsilon\varepsilon_0\kappa_i a_{\text{e},m} I'_m(\kappa_i R) \end{aligned}$$

$$-\frac{mq_z}{R}c_{e,m}I_m(\kappa_i R)\Big] e^{im\phi},$$

whereas the induced electric and magnetic fields outside the cylinder ( $R > a$ ) in vacuum are:

$$\begin{aligned} E_{\text{out},z}(R, \phi, q_z, \omega) &= \sum_{m=-\infty}^{\infty} -\kappa_o^2 b_{e,m} K_m(\kappa_o R) e^{im\phi}, \\ E_{\text{out},R}(R, \phi, q_z, \omega) &= \sum_{m=-\infty}^{\infty} [iq_z \kappa_o b_{e,m} K'_m(\kappa_o R) \\ &\quad - \frac{\omega \mu_0 m}{R} d_{e,m} K_m(\kappa_o R)] e^{im\phi}, \\ E_{\text{out},\phi}(R, \phi, q_z, \omega) &= \sum_{m=-\infty}^{\infty} \left[ -\frac{mq_z}{R} b_{e,m} K_m(\kappa_o R) \right. \\ &\quad \left. - i\omega \mu_0 \kappa_o d_{e,m} K'_m(\kappa_o R) \right] e^{im\phi}, \\ H_{\text{out},z}(R, \phi, q_z, \omega) &= \sum_{m=-\infty}^{\infty} -\kappa_o^2 d_{e,m} K_m(\kappa_o R) e^{im\phi}, \\ H_{\text{out},R}(R, \phi, q_z, \omega) &= \sum_{m=-\infty}^{\infty} \left[ \frac{m\omega \varepsilon_0}{R} b_{e,m} K_m(\kappa_o R) \right. \\ &\quad \left. + iq_z \kappa_o d_{e,m} K'_m(\kappa_o R) \right] e^{im\phi}, \\ H_{\text{out},\phi}(R, \phi, q_z, \omega) &= \sum_{m=-\infty}^{\infty} [i\omega \varepsilon_0 \kappa_o b_{e,m} K'_m(\kappa_o R) \\ &\quad - \frac{mq_z}{R} d_{e,m} K_m(\kappa_o R)] e^{im\phi}. \end{aligned}$$

In the above expressions we assumed only solutions not diverging at  $R = 0$  and at infinity, and we also defined  $\kappa_i = \sqrt{q_z^2 - \varepsilon \frac{\omega^2}{c^2}}$  and  $\kappa_o = \sqrt{q_z^2 - \frac{\omega^2}{c^2}}$ . The unknown coefficients  $a_{e,m}$ ,  $b_{e,m}$ ,  $c_{e,m}$  and  $d_{e,m}$  are obtained by imposing boundary conditions at the boundaries of the cylinder:

$$H_{\text{in},z}(R_0, 0, q_z, \omega) = H_{\text{out},z}(R_0, 0, q_z, \omega), \quad (\text{D1a})$$

$$\begin{aligned} E_{\text{in},z}(R_0, 0, q_z, \omega) &= E_{\text{out},z}(R_0, 0, q_z, \omega) \\ &\quad + E_{\text{el},z}(R_0, 0, q_z, \omega), \end{aligned} \quad (\text{D1b})$$

$$\begin{aligned} \varepsilon E_{\text{in},R}(R_0, 0, q_z, \omega) &= E_{\text{out},R}(R_0, 0, q_z, \omega) \\ &\quad + E_{\text{el},R}(R_0, 0, q_z, \omega), \end{aligned} \quad (\text{D1c})$$

$$\begin{aligned} H_{\text{in},R}(R_0, 0, q_z, \omega) &= H_{\text{out},R}(R_0, 0, q_z, \omega) \\ &\quad + H_{\text{el},R}(R_0, 0, q_z, \omega). \end{aligned} \quad (\text{D1d})$$

By using the transformation in Eq.((3)) we can obtain the electric and magnetic field produced in the presence of the cylinder due to the magnetic current component with the unknown coefficients redefined to  $a_{m,m}$ ,  $b_{m,m}$ ,  $c_{m,m}$  and  $d_{m,m}$ , that can be evaluated by applying the same boundary conditions as in Eqs. (D1). The loss probability per unit trajectory due to the electric and magnetic current is then given by Eq. (12) and Eq. (13), respectively.

\* Electronic address: [aizpurua@ehu.eus](mailto:aizpurua@ehu.eus)

- <sup>1</sup> R. F. Egerton, *Electron energy-loss spectroscopy in the electron microscope* (Springer Science & Business Media, 2011).
- <sup>2</sup> F. J. García de Abajo, Rev. Mod. Phys. **82**, 209 (2010).
- <sup>3</sup> J. Nelayah, M. Kociak, O. Stéphan, F. J. García de Abajo, M. Tencé, L. Henrard, D. Taverna, I. Pastoriza-Santos, L. M. Liz-Marzán, and C. Colliex, Nat. Physics **3**, 348 (2007).
- <sup>4</sup> M. J. Lagos, A. Trügler, U. Hohenester, and P. E. Batson, Nature **543**, 529 (2017).
- <sup>5</sup> A. A. Govyadinov, A. Konečná, A. Chuvilin, S. Vélez, I. Dolado, A. Y. Nikitin, S. Lopatin, F. Casanova, L. E. Hueso, J. Aizpurua, et al., Nat. Commun. **8**, 95 (2017).
- <sup>6</sup> V. Giannini, A. I. Fernández-Domínguez, S. C. Heck, and S. A. Maier, Chem. Rev. **111**, 3888 (2011).
- <sup>7</sup> M. Pelton, J. Aizpurua, and G. Bryant, Laser Photonics Rev. **2**, 136 (2008).
- <sup>8</sup> A. I. Kuznetsov, A. E. Miroshnichenko, M. L. Brongersma, Y. S. Kivshar, and B. Luk'yanchuk, Science **354**, aag2472 (2016).
- <sup>9</sup> S. Jahani and Z. Jacob, Nat. Nanotechnol. **11**, 23 (2016).
- <sup>10</sup> R. Verre, D. G. Baranov, B. Munkhbat, J. Cuadra, M. Käll, and T. Shegai, Nat. Nanotechnol. (2019).
- <sup>11</sup> A. B. Evlyukhin, S. M. Novikov, U. Zywietz, R. L. Eriksen, C. Reinhardt, S. I. Bozhevolnyi, and B. N. Chichkov, Nano Lett. **12**, 3749 (2012).
- <sup>12</sup> P. Albella, R. Alcaraz de la Osa, F. Moreno, and S. A. Maier, ACS Photonics **1**, 524 (2014).
- <sup>13</sup> J. Cambiasso, G. Grinblat, Y. Li, A. Rakovich, E. Cortés, and S. A. Maier, Nano Lett. **17**, 1219 (2017).
- <sup>14</sup> R. M. Bakker, D. Permyakov, Y. F. Yu, D. Markovich, R. Paniagua-Domínguez, L. Gonzaga, A. Samusev, Y. Kivshar, B. Luk'yanchuk, and A. I. Kuznetsov, Nano Lett. **15**, 2137 (2015).
- <sup>15</sup> T. G. Habteyes, I. Staude, K. E. Chong, J. Dominguez, M. Decker, A. Miroshnichenko, Y. Kivshar, and I. Brener, ACS Photonics **1**, 794 (2014).
- <sup>16</sup> A. E. Miroshnichenko, A. B. Evlyukhin, Y. F. Yu, R. M. Bakker, A. Chipouline, A. I. Kuznetsov, B. Luk'yanchuk, B. N. Chichkov, and Y. S. Kivshar, Nat. Commun. **6**, 8069 (2015).
- <sup>17</sup> A. Y. Frolov, N. Verellen, J. Li, X. Zheng, H. Padubrouska, D. Denkova, M. R. Shcherbakov, G. A. E. Vandenbosch, V. I. Panov, P. Van Dorpe, et al., Nano Lett. **17**, 7629 (2017).
- <sup>18</sup> T. Coenen, J. van de Groep, and A. Polman, ACS Nano **7**, 1689 (2013).
- <sup>19</sup> J. van de Groep, T. Coenen, S. A. Mann, and A. Polman, Optica **3**, 93 (2016).
- <sup>20</sup> Q. Liu, S. C. Quillin, D. J. Masiello, and P. A. Crozier, Phys. Rev. B **99**, 165102 (2019).
- <sup>21</sup> O. Kfir, H. Lourenço-Martins, G. Storeck, M. Sivis, T. R. Harvey, T. J. Kippenberg, A. Feist, and C. Ropers, arXiv preprint arXiv:1910.09540 (2019).
- <sup>22</sup> D. T. L. Alexander, V. Flauraud, and F. Demming-

- Janssen, ACS Nano **15**, 16501–16514 (2021).
- <sup>23</sup> A. F. Cihan, A. G. Curto, S. Raza, P. G. Kik, and M. L. Brongersma, Nat. Photonics **12**, 284 (2018).
- <sup>24</sup> R. Regmi, J. Berthelot, P. M. Winkler, M. Mivelle, J. Proust, F. Bedu, I. Ozerov, T. Begou, J. Lumeau, H. Rigneault, et al., Nano Lett. **16**, 5143 (2016).
- <sup>25</sup> V. Rutckaia, F. Heyroth, A. Novikov, M. Shaleev, M. Petrov, and J. Schilling, Nano Lett. **17**, 6886 (2017).
- <sup>26</sup> M. K. Schmidt, R. Esteban, J. Sáenz, I. Suárez-Lacalle, S. Mackowski, and J. Aizpurua, Opt. Express **20**, 13636 (2012).
- <sup>27</sup> A. Vaskin, S. Mashhadi, M. Steinert, K. E. Chong, D. Keene, S. Nanz, A. Abass, E. Rusak, D.-Y. Choi, I. Fernandez-Corbaton, et al., Nano Lett. **19**, 1015 (2019).
- <sup>28</sup> K. Y. Bliokh, Y. P. Bliokh, S. Savel'ev, and F. Nori, Phys. Rev. Lett. **99**, 190404 (2007).
- <sup>29</sup> S. M. Lloyd, M. Babiker, G. Thirunavukkarasu, and J. Yuan, Rev. Mod. Phys. **89**, 035004 (2017).
- <sup>30</sup> K. Y. Bliokh, I. P. Ivanov, G. Guzzinati, L. Clark, R. Van Boxem, A. Béché, R. Juchtmans, M. A. Alonso, P. Schattschneider, F. Nori, et al., Phys. Rep. **690**, 1 (2017).
- <sup>31</sup> M. Uchida and A. Tonomura, Nature **464**, 737 (2010).
- <sup>32</sup> B. J. McMorran, A. Agrawal, I. M. Anderson, A. A. Herzing, H. J. Lezec, J. J. McClelland, and J. Unguris, Science **331**, 192 (2011).
- <sup>33</sup> A. Béché, R. Van Boksem, G. Van Tendeloo, and J. Verbeeck, Nat. Phys. **10**, 26 (2014).
- <sup>34</sup> E. Mafakheri, A. H. Tavabi, P.-H. Lu, R. Balboni, F. Venturi, C. Menozzi, G. C. Gazzadi, S. Frabboni, A. Sit, R. E. Dunin-Borkowski, et al., Appl. Phys. Lett. **110**, 093113 (2017).
- <sup>35</sup> G. M. Vanacore, G. Berruto, I. Madan, E. Pomarico, P. Biagioli, R. J. Lamb, D. McGrouther, O. Reinhardt, I. Kaminer, B. Barwick, et al., Nat. Materials (2019).
- <sup>36</sup> G. Guzzinati, P. Schattschneider, K. Y. Bliokh, F. Nori, and J. Verbeeck, Phys. Rev. Lett. **110**, 093601 (2013).
- <sup>37</sup> V. Grillo, T. R. Harvey, F. Venturi, J. S. Pierce, R. Balboni, F. Bouchard, G. C. Gazzadi, S. Frabboni, A. H. Tavabi, Z.-A. Li, et al., Nat. Commun. **8**, 689 (2017).
- <sup>38</sup> J. Verbeeck, H. Tian, and P. Schattschneider, Nature **467**, 301 (2010).
- <sup>39</sup> S. Lloyd, M. Babiker, and J. Yuan, Phys. Rev. Lett. **108**, 074802 (2012).
- <sup>40</sup> J. Yuan, S. M. Lloyd, and M. Babiker, Phys. Rev. A **88**, 031801 (2013).
- <sup>41</sup> J. Rusz, J.-C. Idrobo, and L. Wrang, Phys. Rev. B **94**, 144430 (2016).
- <sup>42</sup> R. Juchtmans, A. Béché, A. Abakumov, M. Batuk, and J. Verbeeck, Phys. Rev. B **91**, 094112 (2015).
- <sup>43</sup> D. Ugarte and C. Ducati, Phys. Rev. B **93**, 205418 (2016).
- <sup>44</sup> G. Guzzinati, A. Béché, H. Lourenco-Martins, J. Martin, M. Kociak, and J. Verbeeck, Nat. Commun. **8** (2017).
- <sup>45</sup> M. Zanfognini, E. Rotunno, S. Frabboni, A. Sit, E. Karimi, U. Hohenester, and V. Grillo, ACS Photonics **6**, 620 (2019).
- <sup>46</sup> Z. Mohammadi, C. P. Cole P. Van Vlack, S. Hughes, J. Bornemann, and R. Gordon, Opt. Express **20**, 15024 (2012).
- <sup>47</sup> A. Asenjo-Garcia and F. J. García de Abajo, Phys. Rev. Lett. **113**, 066102 (2014).
- <sup>48</sup> F. J. García de Abajo, Phys. Rev. B **59**, 3095 (1999).
- <sup>49</sup> E. D. Palik, *Handbook of optical constants of solids*, vol. 3 (Academic Press, 1998).
- <sup>50</sup> Y. H. Fu, A. I. Kuznetsov, A. E. Miroshnichenko, Y. Yu, and B. Luk'yanchuk, Nat. Commun. **4**, 1527 (2013).
- <sup>51</sup> J. Yan, P. Liu, Z. Lin, H. Wang, H. Chen, C. Wang, and G. Yang, ACS Nano **9**, 2968 (2015).
- <sup>52</sup> U. Zywietz, M. K. Schmidt, A. B. Evlyukhin, C. Reinhardt, J. Aizpurua, and B. N. Chichkov, ACS Photonics **2**, 913 (2015).
- <sup>53</sup> M. V. Rybin, D. S. Filonov, P. A. Belov, Y. S. Kivshar, and M. F. Limonov, Sci. Rep. **5**, 8774 (2015).
- <sup>54</sup> A. L. Holsteen, S. Raza, P. Fan, P. G. Kik, and M. L. Brongersma, Science **358**, 1407 (2017).
- <sup>55</sup> D. J. Traviss, M. K. Schmidt, J. Aizpurua, and O. L. Muskens, Opt. Express **23**, 22771 (2015).
- <sup>56</sup> D. R. Abujetas, R. Paniagua-Domínguez, and J. A. Sánchez-Gil, ACS Photonics **2**, 921 (2015).
- <sup>57</sup> L. Cao, J. S. White, J.-S. Park, J. A. Schuller, B. M. Clemens, and M. L. Brongersma, Nat. Mater. **8**, 643 (2009).
- <sup>58</sup> X. Bendaña, A. Polman, and F. J. García de Abajo, Nano Lett. **11**, 5099 (2011).
- <sup>59</sup> C. A. Walsh, Phil. Mag. B **63**, 1063 (1991).
- <sup>60</sup> E. Snitzer, J. Opt. Soc. Am. **51**, 491 (1961).
- <sup>61</sup> L. Tong, J. Lou, and E. Mazur, Opt. Express **12**, 1025 (2004).
- <sup>62</sup> F. J. García de Abajo and M. Kociak, Phys. Rev. Lett. **100**, 106804 (2008).
- <sup>63</sup> N. R. Verhart, G. Lepert, A. L. Billing, J. Hwang, and E. A. Hinds, Opt. Express **22**, 19633 (2014).
- <sup>64</sup> Y. Tang and A. E. Cohen, Phys. Rev. Lett. **104**, 163901 (2010).
- <sup>65</sup> X. Yin, M. Schäferling, B. Metzger, and H. Giessen, Nano Lett. **13**, 6238 (2013).
- <sup>66</sup> H.-S. Ee, J.-H. Kang, M. L. Brongersma, and M.-K. Seo, Nano Lett. **15**, 1759 (2015).
- <sup>67</sup> H. Lourenço-Martins, D. Gérard, and M. Kociak, Nature Physics **17**, 598 (2021).
- <sup>68</sup> T. R. Harvey, J. S. Pierce, J. J. Chess, and B. J. McMorran, arXiv preprint arXiv:1507.01810 (2015).
- <sup>69</sup> I. Bialynicki-Birula and Z. Bialynicka-Birula, Phys. Rev. Lett. **118**, 114801 (2017).
- <sup>70</sup> S. M. Barnett, Phys. Rev. Lett. **118**, 114802 (2017).
- <sup>71</sup> A. Wiener, H. Duan, M. Bosman, A. P. Horsfield, J. B. Pendry, J. K. W. Yang, S. A. Maier, and A. I. Fernández-Domínguez, ACS Nano **7**, 6287 (2013).
- <sup>72</sup> S. Raza, N. Stenger, A. Pors, T. Holmgaard, S. Kadkhodazadeh, J. B. Wagner, K. Pedersen, M. Wubs, S. I. Bozhevolnyi, and N. A. Mortensen, Nat. Commun. **5** (2014).